Role of interfacial rheology on fingering instabilities in lifting Hele-Shaw flows

Írio M. Coutinho* and José A. Miranda†
Departamento de Física, Universidade Federal de Pernambuco, CCEN, Recife, Pernambuco 50670-901, Brazil

(Received 3 May 2023; accepted 6 August 2023; published 22 August 2023)

The lifting Hele-Shaw cell setup is a popular modification of the classic, fixed-gap, radial viscous fingering problem. In the lifting cell configuration, the upper cell plate is lifted such that a more viscous inner fluid is invaded by an inward-moving outer fluid. As the fluid-fluid interface contracts, one observes the rising of distinctive patterns in which penetrating fingers having rounded tips compete among themselves, reaching different lengths. Despite the scholarly and practical relevance of this confined lifting flow problem, the impact of interfacial rheology effects on its pattern-forming dynamics has been overlooked. Authors of recent studies on the traditional injection-induced radial Hele-Shaw flow and its centrifugally driven variant have shown that, if the fluid-fluid interface is structured (i.e., laden with surfactants, particles, proteins, or other surface-active entities), surface rheological stresses start to act, influencing the development of the viscous fingering patterns. In this paper, we investigate how interfacial rheology affects the stability as well as the shape of the emerging fingered structures in lifting Hele-Shaw flows, at linear and early nonlinear dynamic stages. We tackle the problem by utilizing the Boussinesq-Scriven model to describe the interface and by employing a perturbative mode-coupling scheme. Our linear stability results show that interfacial rheology effects destabilize the interface. Furthermore, our second-order findings indicate that interfacial rheology significantly alters intrinsically nonlinear morphological features of the shrinking interface, inducing the formation of narrow sharp-tip penetrating fingers and favoring enhanced competition among them.

DOI: 10.1103/PhysRevE.108.025104

I. INTRODUCTION

Structured fluid-fluid interfaces, laden with solid particles, surfactants, polymers, lipid bilayers, proteins, and other types of surface-active agents are central components of many natural, scientific, and engineering processes. Interface rheological effects strongly influence the dynamics in suspensions of bubbles, drops, and capsules [1], emulsions [2], foams [3], biological fluids [4], and many other soft matter materials [5]. In addition, such rheologically complex interfaces can be found in many industrial applications, for instance, those related to food technology [6], enhanced oil recovery [7], and cosmetics [8]. Considering all these scientific and technological implications, it is of great academic and practical importance to try to understand how the complicated rheological processes that arise in such structured interfaces impact their dynamic behavior.

The confinement of surface-active entities to a fluid-fluid interface considerably affects the surface properties of the system, giving rise to interfacial stresses which respond to flow and deformation [9–12]. These factors influence the mechanical properties of the interface, causing it to acquire various rheological features. Specifically, the in-plane friction that arises when the molecules or particles within the interface slither against each other causes viscous dissipation, leading to the emergence of intrinsic surface shear, and dilatational viscosities. As a result of the presence of such inherent interfacial rheology properties, structured fluid-fluid interfaces can provide useful ways to alter the mechanical resistance of fluid-fluid boundaries, either restraining or favoring the development of interfacial instabilities. In fact, with appropriate interfacial rheology, one can control the occurrence of important interfacial deformation phenomena such as coarsening, coalescence, rupture, and breakup [13–17].

Quite recently, researchers have begun to examine the role of interfacial rheology effects on a simple but acclaimed interfacial instability, namely, the Saffman-Taylor (or viscous fingering) problem. This fluid dynamic instability takes place when a less viscous fluid displaces a more viscous one in the confined geometry of a Hele-Shaw cell, a device consisting of two parallel glass plates separated by a small gap. Standard versions of this problem occur in motionless and fixed gap width cells, both in rectangular [18] and radial [19–22] setups. In the popular radial flow arrangement, the less viscous fluid is injected at the center of the cell and pushes the more viscous fluid radially outward. Under these circumstances, the fluid-fluid boundary becomes unstable and deforms, leading to the development of distinctive branching patterns, where fingerlike structures split at their tips. Since the important work by Paterson [20], the radial viscous fingering instability has been extensively scrutinized both experimentally and theoretically and has emerged as an archetypal problem in the area of pattern formation and nonlinear phenomenology (see, for instance, Ref. [19] and references therein).

Irrespective of the large number of studies involving the radial viscous fingering problem during the last few decades,

*irio.menezes@ufpe.br
†jose.mirandant@ufpe.br

the role of surface rheological stresses on the interfacial Saffman-Taylor instability has been largely unexplored. Only very recently, this issue was taken up theoretically by Li and Manikantan [23] and subsequently by Conrado *et al.* [24]. By using the Boussinesq-Scriven model [5,9,25–27] to describe the interface as a Newtonian fluid, possessing intrinsic surface shear and dilatational viscosities, the authors of Ref. [23] performed a linear stability analysis of the problem. Their linear stability results indicated that interfacial rheology effects tend to stabilize the fluid-fluid interface by decreasing the band of linearly unstable modes as well as the growth rate of the most unstable mode. This linear finding suggested an enhanced length-scale selection, causing the authors to expect that interfacial rheology effects could lead to the formation of wider fingers.

While linear stability analysis is a useful tool that provides insight into the stability of the interface to small perturbations, it only leads to an accurate description of interfacial solutions for very short times. Consequently, the purely linear stability analysis executed in Ref. [23] had limited quantitative access to changes in the morphology of the fingered patterns when surface rheological effects are present. This restriction increased the need for a more flexible and accurate perturbative method that could be used to better understand the impact of interfacial rheology on key, intrinsically nonlinear pattern-forming phenomena such as tip splitting [22]. This is precisely what has been done by the authors of Ref. [24]. Conrado *et al.* [24] revisited the problem studied in Ref. [23] and employed a perturbative second-order mode-coupling approach to account for larger interface perturbations occurring at longer times. This allowed them to study early nonlinear stages of the radial Hele-Shaw flow under the presence of interfacial rheology effects. The results presented in Ref. [24] showed that, while at the linear level interfacial rheology effects tend to stabilize the overall growth of the interface, at early nonlinear stages, they do favor the development of the emblematic fingertip-splitting events in radial injection-driven Hele-Shaw flows.

Investigators have also considered the impact of surface rheological stresses on fingering patterns that emerge in an interesting variant of the traditional injection-driven, radial Hele-Shaw flow setup in which the gap between the plates is kept constant but the entire Hele-Shaw cell is rotated [28]. This is known as the rotating Hele-Shaw cell problem [29–32], where centrifugal forces cause a denser inner fluid to be propelled outward, which in turn gives rise to interfacial patterns that are distinct from those generated in conventional injection-induced radial Hele-Shaw flows. The rotating fingering patterns assume a range of morphologies, including teardroplike shapes, thin arms having bulbous ends, and intricate backbone structures. However, the most salient feature of these centrifugally driven patterns is the fact that, instead of the occurrence of fingertip-splitting events, one observes the rising of nonsplitting fingered structures markedly characterized by finger length variability. Indeed, the most conspicuous pattern-forming growth phenomenon in rotating Hele-Shaw flows is finger competition (i.e., competition among fingers of different lengths).

Motivated by the rich dynamical and morphological scenarios encountered in the rotating Hele-Shaw cell problem, Coutinho *et al.* [28] used both linear and second-order weakly nonlinear (WNL) analyses to try to understand how these behaviors would be affected by the action of interfacial rheology effects. At the linear level, it has been found that the presence of surface rheological stresses induces interface stabilization and reduces the number of emerging fingers. Moreover, their WNL findings showed that interfacial rheology effects significantly influence the shape of the fingers and their competition dynamics. They have observed that finger competition behaviors result from a complicated joint action of the viscosity contrast of the bulk fluids and the rheological properties of the structured interface. Specifically, it has been found that the competing fingers tend to get increasingly wider as interfacial rheology effects become more intense.

In this paper, we study the impact of interfacial rheology effects on yet another variation of the traditional injection-mediated radial viscous fingering problem. Here, we focus on the *lifting* version of the radial fingering problem in a variable-gap cell [33–43]. The lifting configuration offers an alternative way of generating fingering patterns, for example, by stretching a very thin layer of a more viscous fluid surrounded by a less viscous fluid, both sandwiched between the plates of the Hele-Shaw cell [33,36,37,39,42]. In this setting, the cell gap varies with time, i.e., the upper cell plate is lifted uniformly, while the lower plate remains at rest. As the plates separate, the outer less viscous fluid enters the system, and the more viscous inner fluid moves inward to conserve volume. Consequently, due to the Saffman-Taylor instability, the fluid-fluid interface rapidly deforms, forming eye-catching patterns which are quite different from those obtained in both the injection-induced and rotating Hele-Shaw cell configurations. Experiments and numerical simulations show the formation of interfacial patterns in which nonsplitting invading fingers move inward and compete among themselves. While moving toward the center of the cell, these invading fingers get wider at their tips. Following a period of intense instability, the number of fingers starts to decrease, and for even longer times, the shrinking fluid-fluid interface eventually recircularizes due to capillary effects. It is worth noting that fluid flow in lifting cells is not only of academic relevance but also of significant importance to practical problems in adhesion science [36–38,44,45] and microfluidics [46,47].

Considering the scholarly and pragmatic relevance of confined lifting flows, and stimulated by the recent results obtained in Refs. [23,24,28] regarding the significant impact of interfacial rheology effects on the viscous fingering instability in radial (injection-driven) and rotating (centrifugally induced) Hele-Shaw cell problems, in this paper, we study how surface rheological stresses affect the emergence and time evolution of interfacial patterns in lifting Hele-Shaw cells.

The rest of this paper is organized as follows. Section II presents our second-order perturbative mode-coupling approach. We derive a nonlinear differential equation that describes the time evolution of the interface perturbation amplitudes under lifting Hele-Shaw flow circumstances, considering the action of surface rheological effects. Such a differential equation has a first-order piece involving a relatively simple linear dispersion relation and a second-order part containing a more complicated nonlinear contribution. In Sec. III, we concentrate our attention on the role played

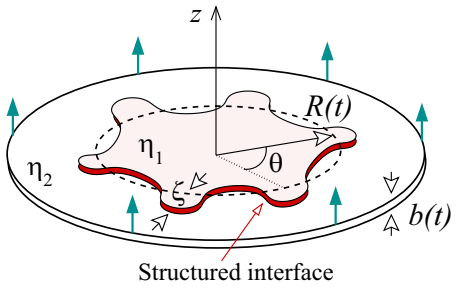

FIG. 1. Schematic diagram of a lifting Hele-Shaw cell with time-dependent gap width $b(t)$, where the inner (outer) fluid has viscosity η_1 (η_2). The fluids are separated by a structured interface. The unperturbed time-dependent interface (dashed curve) is a circle of radius $R = R(t)$, and the interface perturbation is denoted by $\zeta = \zeta(\theta, t)$, where θ is the polar angle. The direction of lifting is along the z axis.

by the Boussinesq number (a controlling parameter that measures the relative strength of surface viscous stresses to bulk viscous stresses) in determining the linear stability behavior of the structured interface as well as the most prevalent morphological features of the interfacial patterns at the onset of nonlinearities.

The purely linear stability aspects of the system are examined in Sec. III A. Our linear stability results show that interfacial rheology effects increase the band of unstable modes, the maximum growth rate, and the corresponding wave number of maximum growth. These observations suggest that, at the linear level, surface rheological stresses act to destabilize the interface. These linear findings for the lifting Hele-Shaw flow system are in contrast to the corresponding linear results obtained in Refs. [23,24,28] for injection-induced radial fingering and rotating Hele-Shaw flows for which interfacial rheology has a stabilizing role.

The influence of interfacial rheology on the development of nonlinear pattern-forming structures is discussed in Sec. III B. We focused on trying to understand how the morphology of the emerging fingers and their finger competition behavior are impacted by the presence of surface rheological stresses. We found that, in lifting Hele-Shaw flows, stronger interfacial rheology effects make the invading fingers sharper at their tips. Once again, this is completely different from the results obtained by previous early nonlinear studies, where interface rheology effects favored the occurrence of fingertip-broadening and splitting events in radial flows driven by injection [24] and the rising of patterns having wide fingers with rounded tips in rotating Hele-Shaw cells [28]. Furthermore, we have detected that the competition of inward-moving fingers becomes more intense when the Boussinesq number is augmented. Finally, in Sec. IV, we briefly summarize our main findings and provide some concluding remarks.

II. BASIC EQUATIONS AND THE SECOND-ORDER MODE-COUPLING DYNAMICS

The physical system we examine is constituted by a lifting Hele-Shaw cell of a variable gap width $b(t)$ containing a more viscous fluid of viscosity η_1 surrounded by a less viscous fluid of viscosity η_2 (see Fig. 1). The fluids are Newtonian, incompressible, and immiscible. We focus on the viscosity-difference-driven unstable motion of the two-fluid interface, where $\eta_2 < \eta_1$. The structured interface separating these bulk fluids is described by the Boussinesq-Scriven model [5,9,23–27] and viewed as a continuous isotropic Newtonian fluid with surface tension γ, intrinsic surface shear viscosity η_s, and intrinsic surface dilatational viscosity κ_s. In this framing, the upper Hele-Shaw cell plate is allowed to move up along the z axis, which is perpendicular to the cell plates, while the lower plate is held fixed at $z = 0$. The initial fluid-fluid interface is circular, having radius $R_0 = R(t = 0)$ and initial gap thickness $b_0 = b(t = 0)$. As the upper plate is moved upward, the outer fluid 2 is sucked in, and the initially circular fluid-fluid boundary retracts. Due to volume conservation, the time-dependent radius of the contracting unperturbed interface is given by

$$R(t) = R_0\sqrt{\frac{b_0}{b(t)}}. \tag{1}$$

From this expression, one can readily see that the velocity of the contracting unperturbed interface $\dot{R}(t) = dR/dt$ is related to the upper plate-lifting velocity along the z axis, $\dot{b}(t) = db/dt$, by the relation $\dot{R}(t) = -(\dot{b}R)/(2b)$.

During the plate-lifting process, the less viscous outer fluid pushes the more viscous inner fluid, and due to the Saffman-Taylor instability, the fluid-fluid boundary deforms. In the context of our mode-coupling perturbative scheme, we describe the distorted fluid-fluid interface as $\mathcal{R}(\theta, t) = R(t) + \zeta(\theta, t)$, where $\zeta(\theta, t) = \sum_{n=-\infty}^{+\infty} \zeta_n(t)\exp(in\theta)$ represents the net interface perturbation in polar coordinates (r, θ) with complex Fourier mode amplitudes $\zeta_n(t)$ and integer wave numbers n. In the Fourier expansion of ζ, we include the $n = 0$ mode to maintain the area of the perturbed shape independent of the perturbation ζ. Contrary to usual purely linear stability analyses (which are first-order in ζ), here, our main goal is to find a differential equation which describes the time evolution of the perturbation amplitudes $\zeta_n(t)$ accurate to second-order in ζ. Therefore, in addition to investigating the linear stability of the structured interface, we can examine how inherently nonlinear morphological aspects of the fingering patterns are affected by interfacial rheology effects.

Before proceeding, we point out that the WNL mode-coupling scheme we use in this paper has been validated over the years by fully nonlinear numerical simulations for various other types of Hele-Shaw flow systems [48–57]. These fully nonlinear investigations used several numerical methods, including spectral, boundary-integral, phase-field, and diffuse-interface approaches, and found that the WNL theory can correctly capture the onset of pattern formation, providing a reliable way to predict various fundamentally important fully nonlinear pattern-forming effects. Likewise, the WNL theory employed in this paper can be utilized to get insight into the fully nonlinear fingering patterns that arise in lifting Hele-Shaw cells when interfacial rheology effects are present.

Fluid flow in the effectively two-dimensional geometry of a lifting Hele-Shaw cell is governed by the gap-averaged Darcy's law [18,19]:

$$\mathbf{v}_j = -\frac{b^2(t)}{12\eta_j}\nabla p_j, \tag{2}$$

and by the gap-averaged modified incompressibility condition [33,36]:

$$\nabla \cdot \mathbf{v}_j = -\frac{\dot{b}(t)}{b(t)}, \tag{3}$$

where $\mathbf{v}_j = \mathbf{v}_j(r,\theta)$ and $p_j = p_j(r,\theta)$ represent the velocity and pressure in fluids $j = 1, 2$, respectively. Since Hele-Shaw flows involve fluid displacements in the very low Reynolds number limit [18,19], the use of Darcy's law [Eq. (2)] requires that the upper Hele-Shaw cell plate is not lifted fast enough to promote any inertial effects. Additionally, as also required in Hele-Shaw flow systems, one must consider that, during the lifting process, the cell gap width is always far smaller than a characteristic length scale in the plane of the cell, which one can take as the unperturbed droplet radius. Thus, the system should remain of large aspect ratio, where $R(t)/b(t) \gg 1$. As in previous experimental and theoretical studies in lifting Hele-Shaw flows [33,36,37,39], we consider that the upper plate is moved with a constant lifting speed $\dot{b} = V$ along the z axis, so that the gap width grows linearly with time as $b = b(t) = b_0 + Vt$.

From Eq. (3), we see that the velocity potentials ϕ_j ($\mathbf{v}_j = -\nabla\phi_j$) obey a Poisson equation $\nabla^2\phi_j = \dot{b}(t)/b(t)$, with solution given by [20,22,33,58]

$$\phi_j = \frac{\dot{b}r^2}{4b} + \sum_{n\neq 0} \phi_{jn}(t)\left(\frac{r}{R}\right)^{(-1)^{(j+1)}|n|} \exp(in\theta). \tag{4}$$

To obtain the equation of motion for the two-fluid interface at $r = \mathcal{R}$ conveniently expressed in terms of the velocity potentials ϕ_j, we rewrite Darcy's law [Eq. (2)] for each of the fluids in terms of ϕ_j and then subtract the resulting equations from each other to get

$$A\left(\frac{\phi_1+\phi_2}{2}\right)\Big|_{r=\mathcal{R}} - \left(\frac{\phi_1-\phi_2}{2}\right)\Big|_{r=\mathcal{R}} = -\frac{b^2(p_1-p_2)|_{r=\mathcal{R}}}{12(\eta_1+\eta_2)}, \tag{5}$$

where $A = (\eta_2 - \eta_1)/(\eta_2 + \eta_1)$ is the viscosity contrast.

To calculate the nonlinear differential equation for the perturbation amplitudes $\zeta_n(t)$, we need to substitute Eq. (4) into the equation of motion for the interface [Eq. (5)], keep second-order terms in the perturbation amplitudes, and Fourier transform them. However, we must still cope with the pressure difference term $(p_1 - p_2)$ at the interface which appears on the right-hand side of Eq. (5) and express it in terms of the perturbation amplitudes. Additionally, note that it is still necessary to write the velocity potential amplitudes $\phi_{jn}(t)$ of Eq. (4) in terms of $\zeta_n(t)$. To accomplish these tasks, we have to specify two fundamental boundary conditions of our problem at the interfacial boundary $r = \mathcal{R}$.

First, we consider a generalized Young-Laplace pressure boundary condition. It is precisely this boundary condition that introduces the contributions coming from the rheological structured interface. It reads

$$\begin{aligned}(p_1 - p_2)_{\mathcal{R}} = {} & \gamma\mathcal{K} + \mathbf{n}\cdot\{\eta_1[\nabla\mathbf{v}_1 + (\nabla\mathbf{v}_1)^T] \\ & - \eta_2[\nabla\mathbf{v}_2 + (\nabla\mathbf{v}_2)^T]\}_{\mathcal{R}}\cdot\mathbf{n} \\ & + (\kappa_s + \eta_s)\left[\boldsymbol{\nabla}_s\cdot\left(\frac{\mathbf{v}_1+\mathbf{v}_2}{2}\right)_{\mathcal{R}}\right]\mathcal{K},\end{aligned} \tag{6}$$

where $\mathcal{K}$ is the interface curvature in the plane of the Hele-Shaw cell, T denotes a matrix transpose, and $\boldsymbol{\nabla}_s = (\mathbf{I} - \mathbf{nn})\cdot\boldsymbol{\nabla}$ is the surface gradient operator. The first term on the right-hand side of Eq. (6) is related to surface tension effects and is the simplest version of the Young-Laplace equation used in Hele-Shaw cell problems [18,19]. The second term originates from the balance of viscous normal stresses at the interface [59,60], while the last term arises from the action of interfacial rheology effects [23,24].

The last term in Eq. (6) is of key importance to our current study. A version of it was proposed by Li and Manikantan [23], who assumed a simplified situation in which, at the interface, the unit normal vector was directed only along the radial direction. Then Conrado *et al.* [24] derived an improved version of the Young-Laplace condition [the one shown in Eq. (6)], incorporating the role of interfacial rheology effects under more general circumstances, where the unit normal vector at the interface pointed in an arbitrary direction. Moreover, unlike Li and Manikantan [23], they assumed that the velocity at the structured interface was given by the average of the inner and outer fluid velocities. In both in Refs. [23,24], the authors employed the Boussinesq-Scriven model [5,9,23–27] and described the structured interface separating the bulk fluids 1 and 2 as being a compressible Newtonian fluid with intrinsic surface shear (η_s) and dilatational (κ_s) viscosities.

Within this theoretical framework, the authors of Refs. [23,24] considered Cauchy's momentum conservation equation at the interface, in a low Reynolds limit, and with spatially uniform surface tension γ between the fluids. In this way, inertial and Marangoni's stress contributions were safely neglected. Substituting the surface stress tensor given by Scriven's generalization of the Newtonian approximation for the interface proposed by Boussinesq in Cauchy's equation, after fairly lengthy calculations and numerous mathematical manipulations, Eq. (6) is obtained. For more information about the multiple steps leading to Eq. (6), we refer the reader to the detailed derivations presented in Refs. [23,24].

Note that, throughout this paper, to better relate our results to existing articles in Hele-Shaw lifting flows [33,36,37,39,58], we choose to aim attention at the largely explored situation in which the inner fluid is much more viscous than the outer one (i.e., $\eta_1 \gg \eta_2$ or $A = -1$). Furthermore, our theoretical study is also in line with experimental studies that explore different techniques to measure the interfacial shear and dilatational viscosities. The surface shear viscosity η_s is typically measured by tracing particles placed at the interface utilizing interfacial magnetic rods [61], microbutton rheometers [62], and Couette rheometers [63]. Representative values of η_s can vary from $<10^{-9}$ to 10^{-3} N s/m. On the other hand, the dilational shear viscosity κ_s is usually obtained through oscillatory bubble- and drop-based techniques [63,64]. Experimental measurements [65–67] indicate that κ_s is typically two orders of magnitude greater than η_s, being of $O(10^{-1})$ N s/m. Consistent with these experimental facts, and as in Refs. [23,24,28], in this paper, we consider that $\kappa_s \gg \eta_s$.

For the sake of conciseness, in Eq. (6), the contributions of viscous normal stresses and interfacial rheology are both written in terms of the velocities of the fluids $\mathbf{v}_j$. However, these contributions can also be conveniently written in terms of the velocity potentials ϕ_j. For detailed (and long) expressions of

the second and last terms on the right-hand side of Eq. (6) properly expressed in terms of ϕ_j and their derivatives with respect to r and θ, see eqs. (21) and (22) in Ref. [24].

After presenting the generalized Young-Laplace pressure jump condition [Eq. (6)], we now introduce the second relevant boundary condition for our boundary value problem, the so-called kinematic boundary condition [18,19]:

$$\mathbf{n}\cdot\nabla\phi_1 = \mathbf{n}\cdot\nabla\phi_2, \tag{7}$$

which expresses the fact that the normal components of the fluid velocities are continuous across the interface.

At this point, we have all the necessary elements to find a second-order mode-coupling differential equation that describes the time evolution of the interfacial amplitudes $\zeta_n(t)$. We can benefit from the kinematic boundary condition [Eq. (7)] and use it to express the velocity potentials ϕ_j in terms of ζ_n. Substituting the resulting relations from this procedure as well as the generalized pressure jump condition [Eq. (6)] into the equation of motion for the interface [Eq. (5)], always keeping terms up to second order in ζ, and Fourier transforming, we finally obtain the dimensionless, nonlinear differential equation for the perturbation amplitudes $\zeta_n(t)$ (for $n \neq 0$):

$$\dot{\zeta}_n = \lambda(n)\,\zeta_n + \sum_{p\neq 0}\{[F(n,p) + F_{\text{Rheo}}(n,p)]\,\zeta_p\zeta_{n-p} + \lambda(p)[G(n,p) + G_{\text{Rheo}}(n,p)]\zeta_p\zeta_{n-p}\}, \tag{8}$$

where

$$\lambda(n) = \frac{1}{s(n)}\frac{\dot{b}}{2b}\left[(-A|n|-1) - \frac{b^3}{6q^2}|n|(A+|n|) + \frac{b^{7/2}\text{Bq}}{12q^3}|n|(n^2-2)\right] - \frac{b^{7/2}}{s(n)q^3\text{Ca}}|n|(n^2-1) \tag{9}$$

is the linear growth rate, with

$$s(n) = 1 + \frac{b^3}{6q^2}|n|(|n|+A) + \frac{b^{7/2}\text{Bq}}{12q^3}|n|. \tag{10}$$

The second-order mode-coupling terms are

$$F(n,p) = \frac{b^{1/2}}{s(n)}\left(\frac{\dot{b}}{2b}\left\{-A|n|\left[\text{sgn}(np) - \frac{1}{2}\right] - 1\right\} - \frac{b^{7/2}}{q^3\text{Ca}}|n|\left[1 - \frac{p}{2}(3p+n)\right] + \frac{\dot{b}\,b^2}{12q^2}|n|\{A + 3Anp - 2Ap^2 + 3|p| + (n-2p)\text{sgn}(p) - |n|[1 + A\,n\,\text{sgn}(p)]\}\right), \tag{11}$$

$$F_{\text{Rheo}}(n,p) = -\frac{\text{Bq}}{s(n)}\frac{\dot{b}\,b^3}{48q^3}|n|[2n^2\text{sgn}(np) - 2n^2 + np + 7p^2 - 6], \tag{12}$$

$$G(n,p) = \frac{b^{1/2}}{s(n)}\left(A|n|[1-\text{sgn}(np)] - 1 + \frac{b^3}{6q^2}|n|\{A[-n|n|\text{sgn}(p) + 2np - p^2 + 1] - |n| + 3|p| + (n-2p)\text{sgn}(p)\}\right), \tag{13}$$

and

$$G_{\text{Rheo}}(n,p) = -\frac{1}{s(n)}\frac{b^4\text{Bq}}{12q^3}|n|\{n^2[\text{sgn}(np)+1] - 4np + 2p^2 - 2\}. \tag{14}$$

The Rheo subscript indicates the terms that arise purely from interfacial rheology effects. The in-plane lengths, $b(t)$ and time t are rescaled by R_0, b_0, and $b_0/|\dot{b}(0)|$, respectively. By inspecting Eqs. (8)–(14), one verifies that the system is described by the following dimensionless governing parameters:

$$\text{Bq} = \frac{\kappa_s}{(\eta_1+\eta_2)b_0}, \quad q = \frac{R_0}{b_0},$$
$$\text{Ca} = \frac{12(\eta_1+\eta_2)|\dot{b}(0)|}{\gamma},$$

plus the viscosity contrast A (dimensionless viscosity difference between the bulk fluids) which has been defined right after Eq. (5). The parameters listed above are the Boussinesq number Bq, which measures the relative strength of surface to bulk viscous stresses; the global capillary number Ca, which expresses a relative measure of viscous to surface tension forces; and q, representing the initial aspect ratio that quantifies the degree of spatial confinement of the system. Equations (8)–(14) constitute one of the central results of this paper, offering the time evolution of the perturbation amplitudes ζ_n accurate to second order and considering the action of interfacial rheology effects into the lifting Hele-Shaw cell problem.

III. DISCUSSION

A. First order—Linear regime

Although the main focus of this paper is to examine the influence of surface rheology on the morphology of the lifting flow fingering patterns at early nonlinear dynamical stages, a brief discussion about the linear regime can be instructive. Considering Eq. (8) only up to first order, we reduce the problem to the usual linear stability situation, and each mode grows or decays independently of all others. In this way, positive values of $\lambda(n)$ lead to the growth of an unstable interface, and larger $\lambda(n)$ values result in faster growth.

Inspecting the linear growth rate [Eq. (9)], one observes that the first term between the square brackets, which involves the viscosity contrast A, makes the interface unstable if $A < 0$. It is evident that the term related to interfacial rheology

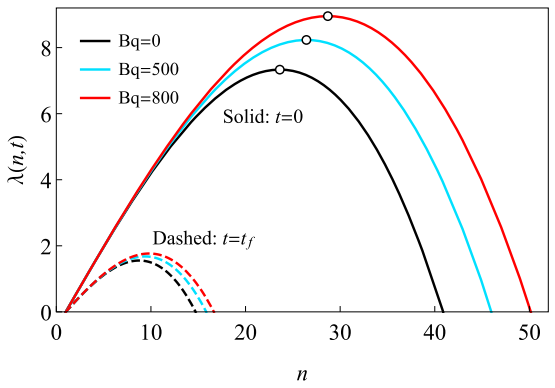

FIG. 2. Linear growth rate $\lambda(n)$ [Eq. (9)] as a function of the wave number n for Bq $= 0$, 500, and 800. Solid curves indicate the behavior of $\lambda(n)$ at the initial time $t = 0$, and the dashed ones at the final time $t = t_f$. Here, $q = 70$, and Ca $= 1/100$. The maxima of the solid curves are indicated by small open circles to guide the eye. Note that, as Bq is increased, the band of unstable modes [for which $\lambda(n) > 0$] also increases.

effects, proportional to the Boussinesq number Bq, also has a destabilizing role. On the other hand, the contributions from normal viscous stresses (term proportional to b^3) and surface tension (term proportional to $1/\mathrm{Ca}$) act to stabilize the interface.

To better illustrate our main linear findings, in Fig. 2, the linear growth rate $\lambda(n)$ is plotted against the wave number n for three values of the Boussinesq number Bq: 0, 500, and 800. The solid curves depict $\lambda(n)$ at the beginning of the evolution $t = 0$, while the dashed curves display the equivalent behavior at the final time $t = t_f = 0.56$. All this is obtained by considering $\mathrm{Ca} = \frac{1}{100}$ and $q = 70$.

From Fig. 2, one can see that, for a given time, larger values of Bq increase the maximum growth rate [$\lambda(n = n_{\max})$] as well as the corresponding wave number $n_{\max}$. In addition, it is clear that the band of unstable modes also increases as Bq is augmented. As the typical wavelength of the system is given by $\Lambda = 2\pi R(t)/n_{\max}$, and since $n_{\max}$ increases with Bq, stronger surface rheological effects lead to smaller wavelengths. This indicates the enhanced development of narrower fingered structures.

Our findings are in stark contrast to the linear results obtained in Refs. [24,28], where injection- and centrifugally driven flows were considered under the presence of interfacial rheology effects. In these studies, it has been found that, at the linear regime, increasingly larger surface rheology effects lead to a decreased maximum growth rate and to smaller maximum wave numbers. Therefore, in Refs. [24,28], at the linear level, larger Bq tends to suppress interfacial instabilities. Nevertheless, in our lifting Hele-Shaw flow system, the effect of surface rheological stresses is just the opposite. This can be justified as follows. Note that, in Refs. [24,28], the inner fluid pushes the outer fluid outward, causing the fluid-fluid boundary to expand. However, in our current lifting flow case, the direction of fluid flow is reversed, in such a way that the outer fluid displaces the inner one, causing the fluid-fluid interface to move inward and contract. By scrutinizing the generalized Young-Laplace condition [Eq. (6)], one verifies that the surface rheological contribution is proportional to the surface divergent of the velocity field. Consequently, if the fluid flow direction is inverted, the role played by interfacial rheology effects is reversed. This also justifies another noteworthy difference between our linear predictions and the ones made in Refs. [24,28]: While in injection- and centrifugally induced flows interfacial rheology effects favor the production of wider fingers, in lifting flows, surface rheology acts to promote the emergence of narrower fingers.

By examining Fig. 2, one can see that, as time progresses from $t = 0$ to t_f, the curves representing the linear growth rate tend to shrink in height and width, favoring an overall interface stabilization and progressively diminishing the number of fingers generated at the interface. Eventually, this would lead to a recircularization of the contracting interface, in which $\lambda(n)$ is so small that all the fingers at the interface vanish. In fact, this linearly predicted recircularization effect has been detected both numerically [33] and experimentally [39] for systems with small enough capillary numbers and when no interfacial rheology effect is present. Considering the destabilizing role of interfacial rheology effects illustrated in Fig. 2, it is reasonable to speculate that larger values of Bq would tend to delay the occurrence of such droplet recircularization phenomena.

B. Second order—Early nonlinear regime

To analyze the impact of interfacial rheology on the pattern formation process at the onset of nonlinearities, we must go beyond linear stability analysis. By considering the full scope of the mode-coupling equation [Eq. (8)], we can probe into early nonlinear effects [22], allowing us to investigate how the shape of the fingers and the competition among them react to the action of surface rheological stresses.

We start by rewriting the net perturbation on the interface in terms of cosine and sine modes:

$$\zeta(\theta, t) = \zeta_0 + \sum_{n=1}^{\infty} [a_n(t)\cos(n\theta) + b_n(t)\sin(n\theta)], \tag{15}$$

where $a_n(t) = \zeta_n(t) + \zeta_{-n}(t)$ and $b_n(t) = i[\zeta_n(t) - \zeta_{-n}(t)]$ are real-valued functions. Mass conservation imposes

$$\zeta_0 = -\frac{1}{4R} \sum_{n=1}^{\infty} \left[a_n^2(t) + b_n^2(t)\right]. \tag{16}$$

To investigate the fingering patterns in general and realistic conditions, we follow the model proposed by Cardoso and Woods [21] that considers aspects of real experiments in Hele-Shaw flows. This model explores the effects of background level noise that can arise from thermal and pressure fluctuations and inhomogeneities on the plates of the cell [68]. To model the noise, each Fourier mode n is assigned a random complex amplitude $\zeta_n(0)$, independent of n.

Under these conditions, in Fig. 3, we solve Eq. (8) up to first [Figs. 3(a)–3(c)] and second [Figs. 3(d)–3(f)] order, considering the participation of modes $2 \leqslant n \leqslant 60$ and taking $|\zeta_n(0)| = \frac{1}{1700}$. As the role of the capillary number Ca in lifting Hele-Shaw flows is already well known (see, for instance, Refs. [33,39,58]), throughout this paper, we focus on understanding how the Boussinesq number Bq affects the

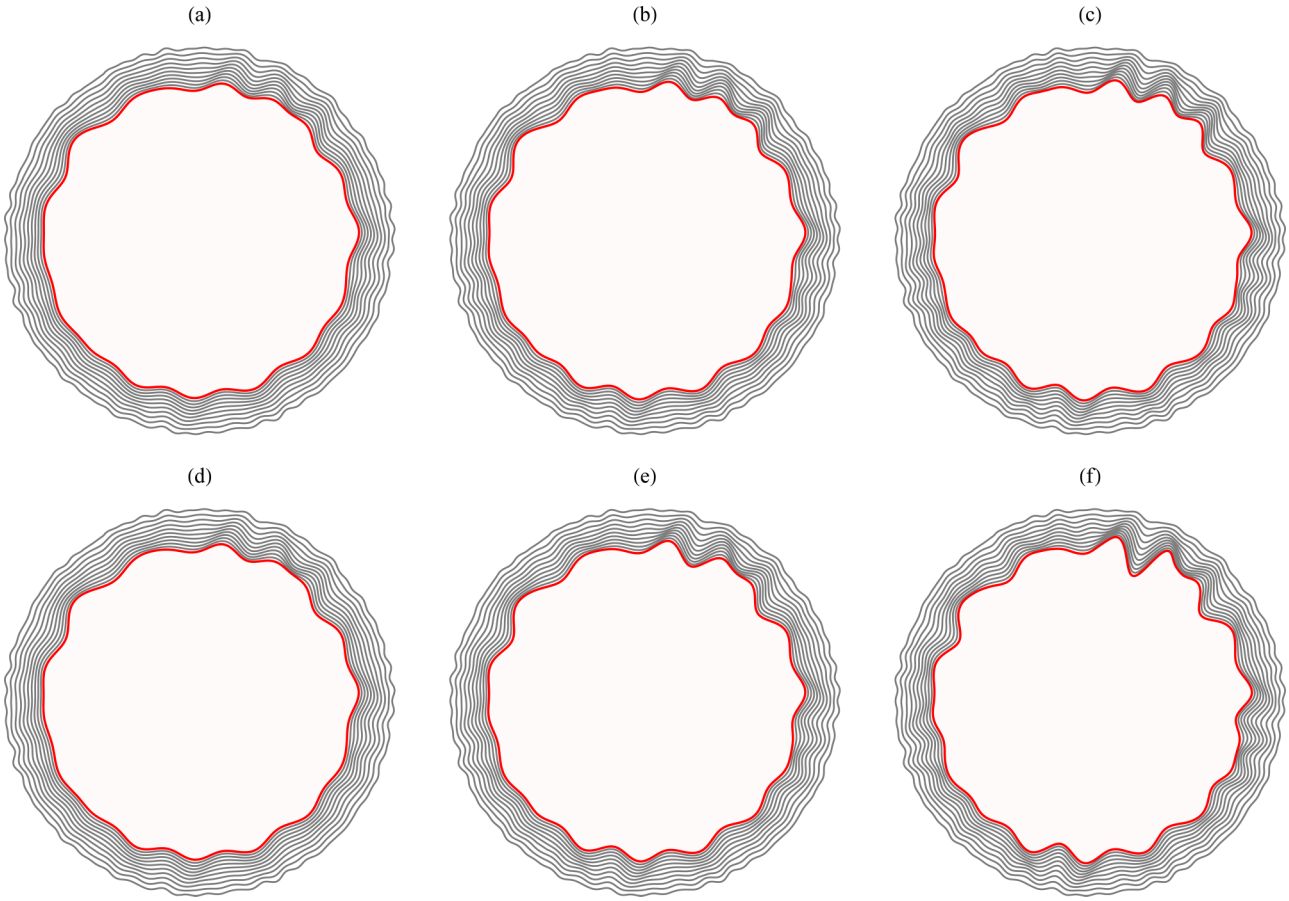

FIG. 3. Time evolution of characteristic interfacial patterns in the presence of background noise, for a range of participating Fourier modes $2 \leqslant n \leqslant 60$ and $0 \leqslant t \leqslant t_f$. The patterns are obtained by solving Eq. (8) up to (a)–(c) first and (d)–(f) second order. We take $q = 70$, $\mathrm{Ca} = 1/100$, $t_f = 0.56$, and three values of Bq: (a) and (d) $\mathrm{Bq} = 0$, (b) and (e) $\mathrm{Bq} = 500$, and (c) and (f) $\mathrm{Bq} = 800$.

system for different values of the initial aspect ratio q. In this framing, Fig. 3 depicts the time evolution of typical linear [Figs. 3(a)–3(c)] and WNL [Figs. 3(d)–3(f)] pattern-forming structures for three values of the Boussinesq number: $\mathrm{Bq} = 0$ [(a) and (d)], $\mathrm{Bq} = 500$ [(b) and (e)], and $\mathrm{Bq} = 800$ [(c) and (f)]. The patterns are presented for $0 \leqslant t \leqslant t_f$, where the various interfaces of each pattern are plotted in equal time intervals of $t_f/10$. Furthermore, $\mathrm{Ca} = \frac{1}{100}$, $q = 70$, and $t_f = 0.56$.

During the course of our work, we paid close attention to the limit of validity of our perturbative theory in such a way that, for each time t considered, we always make sure that interface perturbations $|\zeta(\theta, t)|$ are considerably smaller than the associated unperturbed interface radius $R(t)$. In other words, our perturbative WNL approach requires that $|\zeta(\theta, t)|/R(t) \ll 1$. Therefore, in all calculations and plots presented in this paper, we adopted a validity criterion for which $|\zeta(\theta, t_f)| \approx 12\%$ of $R(t_f)$, where $t_f = 0.56$ is the final time considered for the evolution of the interfacial patterns (i.e., the largest time for which our perturbative approach remains valid).

As already discussed in Secs. I and II, the choice for the viscosity contrast we use is made to eventually facilitate a connection with previous lifting Hele-Shaw cell studies, as most of them consider the case in which $A = -1$. For the sake of clarity, we briefly comment on the chosen representative value for the capillary number Ca we utilize to present our results. From previous works, it is known that, if Ca is too small, only very small perturbations form at the interface, leading to the rise of patterns that are morphologically uninteresting. On the other hand, if Ca is too large, the interface becomes highly perturbed in very short times, making the situation unsuitable to be described perturbatively. For lifting Hele-Shaw cell flows, the capillary number varies in the range $O(10^{-3}) \leqslant \mathrm{Ca} \leqslant O(10)$ [33,39]. Considering the fact that interfacial rheology effects tend to enhance the growth of the fingers, we must use a relatively small capillary number $\mathrm{Ca} = \frac{1}{100}$ to compare the cases without ($\mathrm{Bq} = 0$) and with ($\mathrm{Bq} > 0$) interfacial rheology still within the validity limits of our perturbative scheme. The impact of varying initial aspect ratios q on the lifting system will be explored later in this paper.

We begin by analyzing the first-order patterns [Figs. 3(a)–3(c)]. When surface rheological stresses are absent [Fig. 3(a)], one detects the formation of a slightly perturbed interface, having short and wide fingers that move inward as time advances. Conversely, as surface rheological stresses are considered [Figs. 3(b) and 3(c)], as predicted by the analysis of the linear growth rate, larger Boussinesq numbers result in more deformed interfaces. While one can notice that the

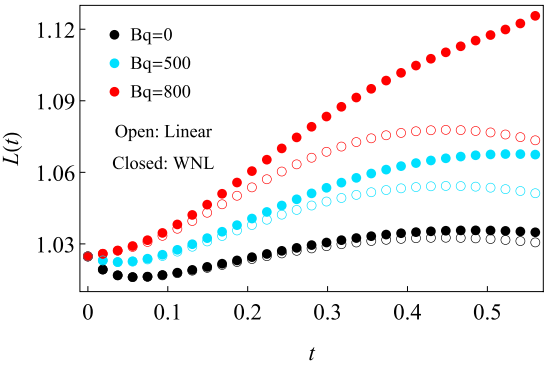

FIG. 4. Time evolution of the rescaled interfacial perimeter $L(t)$ [Eq. (17)] for the patterns presented in Fig. 3, and three increasing values of the Boussinesq number Bq. Open dots represent data from the linear interfaces [Figs. 3(a)–3(c)] and closed dots from the weakly nonlinear ones [Figs. 3(d)–3(f)].

interfaces become progressively more perturbed as the Bq is increased, the morphological changes among these linear patterns are not really significant.

To investigate how nonlinear effects influence the morphology of the generated patterns under the presence of increasingly stronger interfacial rheology effects, we turn our attention to the WNL patterns portrayed in Figs. 3(d)–3(f). When Bq = 0 [Fig. 3(d)], the resulting pattern is just mildly deformed, having short and wide fingers. Therefore, when Bq = 0, the nonlinear effects are barely manifested, leading to a WNL structure that is quite similar to its linear counterpart [Fig. 3(a)]. Nonetheless, by considering the Boussinesq number Bq = 500 [Fig. 3(e)], we see that the produced nonlinear pattern is clearly distinct from the one generated for Bq = 0 in Fig. 3(d). In Fig. 3(e), the fingers are more developed and of more variable sizes, indicating an enhanced finger competition.

Further increasing Bq to 800 [Fig. 3(f)], one verifies that the fingers are even more developed, exhibiting greater finger length variability. The difference in the morphologies of the fingers in the WNL structures shown in Figs. 3(d)–3(f) is also noticeable, as the inward-moving fingers become increasingly sharper whenever surface rheological effects become more intense. Moreover, by contrasting linear [Figs. 3(a)–3(c)] and WNL [Figs. 3(d)–3(f)] patterns, the importance of including nonlinear effects to better capture the role played by interfacial rheology on the dynamics and shape of lifting Hele-Shaw cell patterns is apparent. From these lifting flow results, we conclude that surface rheological stresses act to destabilize the structured interface, leading to the development of faster finger growth, enhanced finger competition, and sharper fingertips.

To complement our analysis, Fig. 4 plots the time evolution of the rescaled interfacial perimeter:

$$L(t) = \frac{1}{2\pi R(t)} \int_0^{2\pi} \sqrt{\mathcal{R}^2(\theta,t) + \left[\frac{d\mathcal{R}(\theta,t)}{d\theta}\right]^2}\, d\theta \qquad (17)$$

for the linear and WNL interfaces presented in Fig. 3. Here, $L(t)$ is the ratio of the length of the perturbed interface to the circumference of the corresponding unperturbed circle of radius $R(t)$. The rescaled perimeter is a convenient way to capture the departure from a circular interface and the increase in complexity of the patterns as Bq is enlarged. In general, the perimeter starts to increase once the fingering instability is triggered. Therefore, an earlier growth and a higher rate of growth of $L(t)$ reflect a more unstable interface.

From Fig. 4, one can see that, for the linear patterns (whose behavior is indicated by open dots in Fig. 4), the behaviors of the interfacial perimeter for the three values of Bq follow similar trends: Essentially, at first, $L(t)$ increases, reaches a maximum, and then decreases. This characteristic behavior is related to the recircularization events mentioned at the end of Sec. III A. Therefore, after an initial period of intense interface deformation, the contracting interface stabilizes due to surface tension effects, and for long times, it eventually tends to an almost perfect circle. Despite these similarities, one can also notice from Fig. 4 that the curves formed by the open dots for larger Bq are located above the ones having lower Bq, showing that stronger interfacial rheology effects induce increased destabilization.

Additionally, by examining the behavior of $L(t)$ for the WNL interfaces (associated with the closed dots in Fig. 4), a general tendency like the one shown by the linear curves is observed: Higher Bq results in a larger perimeter. Nevertheless, it is visible that, as Bq is increased, the nonlinear curves differ more strongly from the linear ones as time progresses. In fact, for a given Bq, one can see that, at a certain time, the slope of the nonlinear curves become higher than the ones for the linear curves. This last feature is especially perceptible for higher values of the Boussinesq number Bq. For example, in Fig. 4, while the WNL curves for Bq = 0 and 500 share the typical rise and fall behavior of the linear curves, the solid dot curve for Bq = 800 does not. The steep curve behavior for Bq = 800 lasts for the whole evolution time, indicating a significant delay in the occurrence of interface recircularization for high enough values of Bq.

To evaluate the robustness of our predictions regarding the change in the initial conditions, in Fig. 5, we present the time evolution of the WNL interfacial patterns for the same physical parameters used in Fig. 3 but now considering two additional sets of random phases. The WNL structures for the first (second) set of additional phases are displayed in Figs. 5(a)–5(c) [Figs. 5(d)–5(f)]. The same values of the Boussinesq number utilized in Fig. 3 are considered: Bq = 0 [(a) and (d)], Bq = 500 [(b) and (e)], and Bq = 800 [(c) and (f)]. By scrutinizing Fig. 5, irrespective of the use of different random phases, one verifies that the main morphological features previously detected in the WNL patterns in Fig. 3 are still present. When no surface rheological stresses are acting (Bq = 0), the patterns illustrated in Figs. 5(a) and 5(d) are just mildly deformed, showing the emergence of small and blunt inward-moving fingers. This is in contrast with the significantly more perturbed structures seen in Figs. 5(c) and 5(f), when interfacial rheology effects take action and are of large magnitude (Bq = 800). The resulting inward-pointing fingered structures for Bq = 800 are notably sharper at their tips and present a greater length variability among them, characterizing an increased finger competition behavior. We point out that we have tested a number of other sets of phases

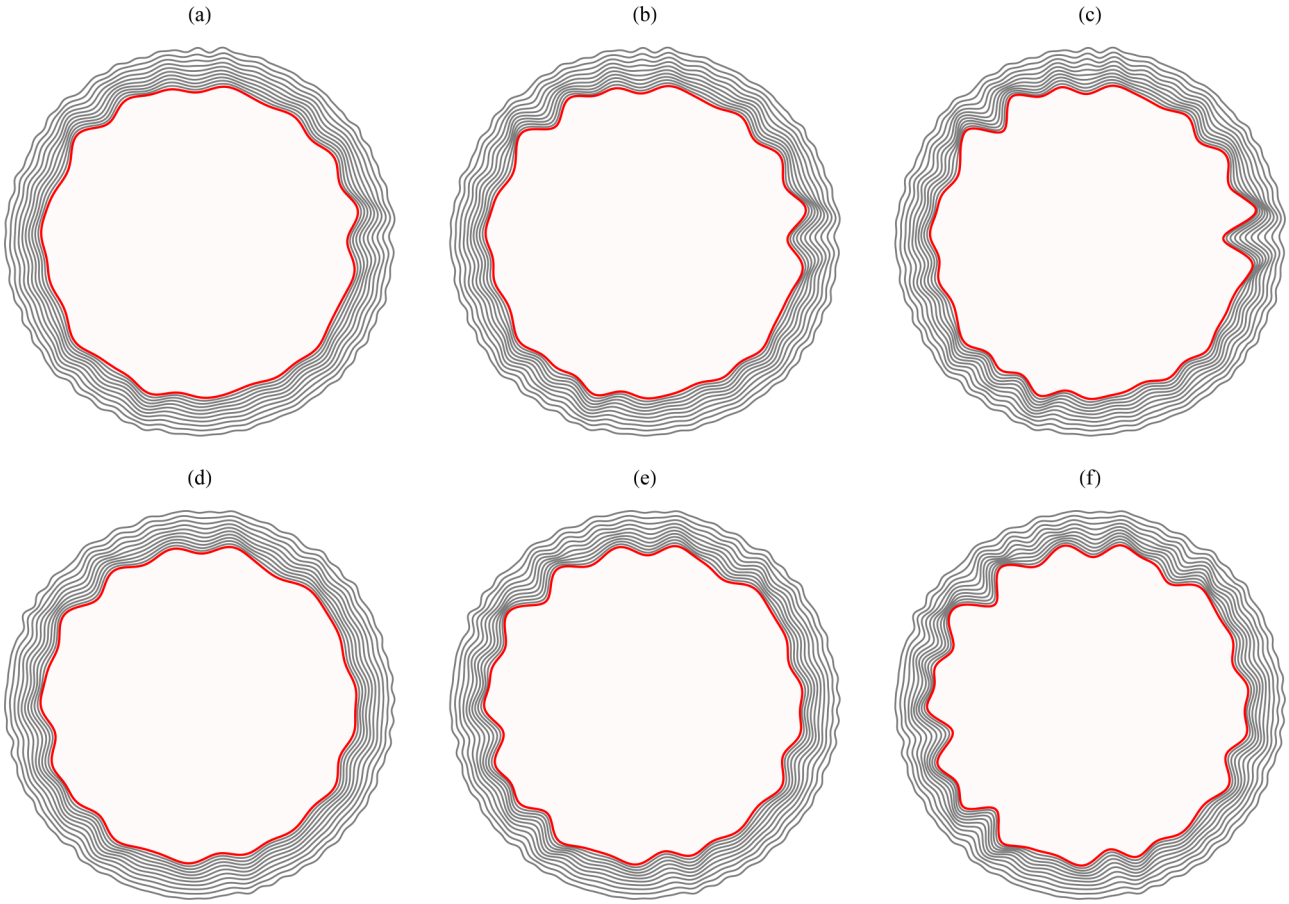

FIG. 5. Representative examples for the time evolution of weakly nonlinear patterns plotted by using initial conditions that are distinct from those in Figs. 3(d)–3(f). Two additional sets of random phases are shown, one for (a)–(c) and another for (d)–(f). However, all physical parameters are the same as the ones employed in Figs. 3(d)–3(f).

and observed dynamical and morphological responses like the ones already unveiled in Figs. 3 and 5.

Up to this point, we have illustrated our results for one representative value of the initial aspect ratio, namely, $q = 70$. However, from existing studies of lifting Hele-Shaw flows in the absence of interfacial rheology effects [33,36,37,39], it is known that the cell confinement parameter q may influence the stability and the shape of the contracting interface. Motivated by these facts, in Fig. 6, we seek to understand how different values of q and Bq affect the system at the early nonlinear regime. In Fig. 6, we present the time evolution of the WNL patterns for three values of the initial aspect ratio $q = 60$ [(a)–(c)], $q = 65$ [(d)–(f)], and $q = 70$ [(g)–(i)] and three values of the Boussinesq number $\mathrm{Bq} = 0$ [(a), (d), and (g)], $\mathrm{Bq} = 500$ [(b), (e), and (h)], and $\mathrm{Bq} = 800$ [(c), (f), and (i)]. The rest of the physical parameters and the initial random phases are identical to those used in Fig. 3. Small black arrows guide the eye to one specific finger where it is easier to perceive the most significant morphological changes.

Before beginning the analysis of Fig. 6, recall that the parameter $q = R_0/b_0$ measures the confinement of the system. For instance, higher values of q, which in lifting Hele-Shaw cell experiments without interfacial rheology effects typically vary within the range $25 \leqslant q \leqslant 120$ [36,37,39], imply small values of the initial cell gap thickness b_0 or relatively large initial unperturbed radius R_0. We start our examination of Fig. 6 by focusing on the patterns generated when interfacial rheology effects are not present $\mathrm{Bq} = 0$ and for three increasing values of the initial aspect ratio: (a) $q = 60$, (d) $q = 65$, and (g) $q = 70$. It is evident that, when surface rheological stresses are not considered (i.e., for $\mathrm{Bq} = 0$), larger values of q lead to more perturbed interfaces. However, it is also clear that, when $\mathrm{Bq} = 0$, small increments in q do not affect the interfacial instability significantly. After all, the pattern shown in Fig. 6(g) for $q = 70$ is just slightly more deformed than the one depicted in Fig. 6(a) for $q = 60$ (see, for instance, the reentrant finger indicated by the small black arrows in the first column of Fig. 6).

Different scenarios are revealed by the lifting patterns produced when interfacial rheology effects are considered and become more intense. For example, from the fingered structures displayed in the second column of Fig. 6, for $\mathrm{Bq} = 500$ [(b), (e), and (h)], one can see that, by increasing the initial aspect ratio from $q = 60$ to 70, it becomes more apparent that larger values of q lead to more intense interfacial perturbations. This behavior is even more noticeable in the third column of Fig. 6 for a larger value of the Boussinesq number $\mathrm{Bq} = 800$ [(c), (f), and (i)]. Observe, for instance, that the finger indicated by the small black arrow in Fig. 6(i) for $q = 70$

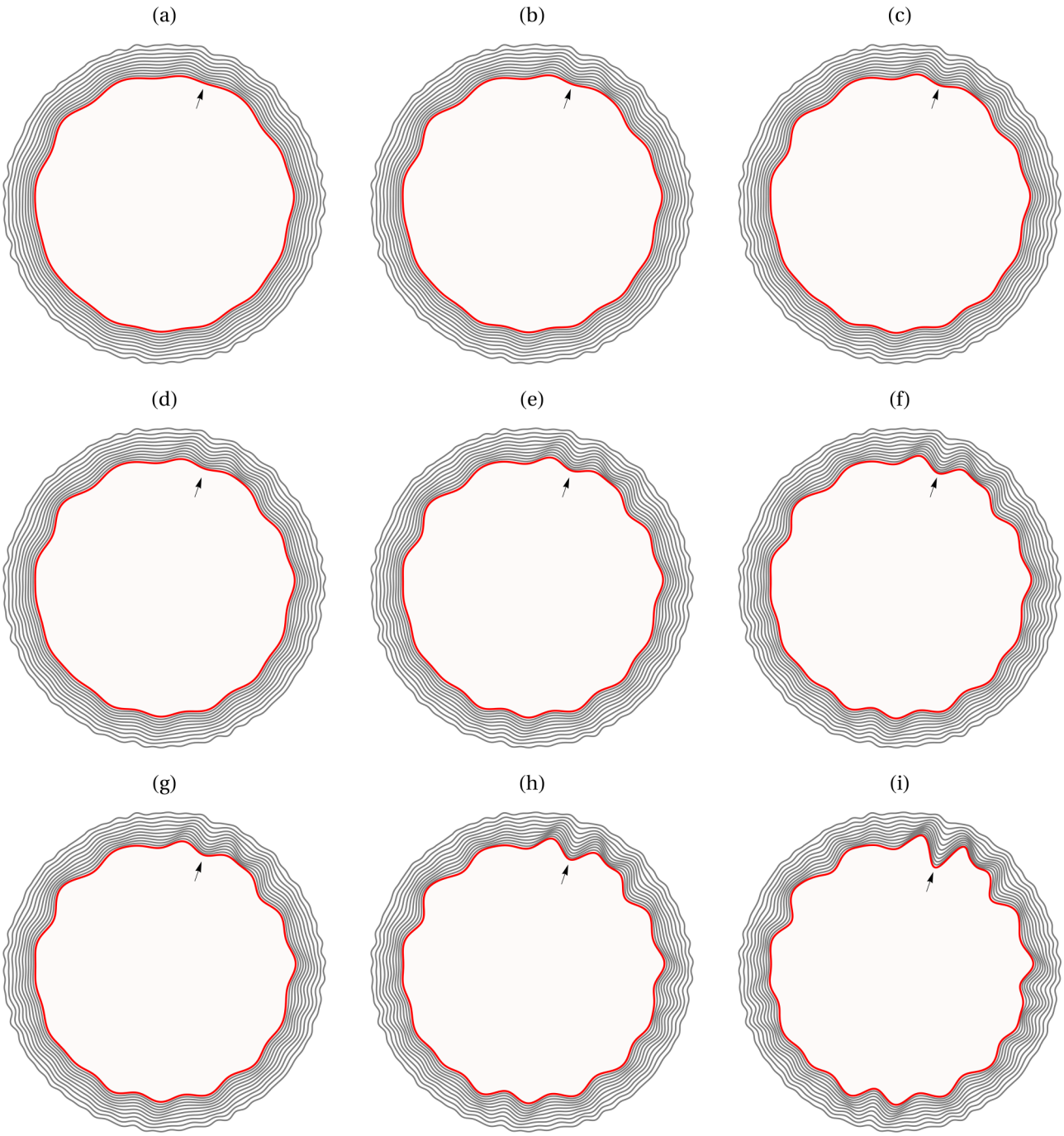

FIG. 6. Time evolution of the weakly nonlinear patterns for (a), (d), and (g) Bq = 0, (b), (e), and (h) Bq = 500, and (c), (f), and (i) Bq = 800. Here, three values of the initial aspect ratio are considered: (a)–(c) $q = 60$, (d)–(f) $q = 65$, and (g)–(i) $q = 70$. All the other physical parameters and initial conditions are equal to those utilized in Fig. 3. Small black arrows are used to help guide the eye to the finger where the most salient shape changes occur.

is longer and sharper than the corresponding finger shown in Fig. 6(c) for $q = 60$. Therefore, from the analysis of Fig. 6, we conclude that higher values of q consistently induce more interfacial instabilities and that this effect strengthens the action of surface rheological stresses. Indeed, higher values of q and Bq lead to more unstable interfaces, whose fingers are sharper and compete more intensively among themselves (increased finger length variability).

It is of interest to investigate in a more quantitative fashion how the shape of the fingertips of the inward-moving fingers of the contracting interface would react to changes in the Boussinesq number Bq. This is done in Fig. 7, which plots the curvature of the fingertip $\mathcal{K}_T$ of the finger identified by the small black arrows in Fig. 6 for the final time t_f, as a function of Bq, and for three values of q. The curvature of the interface, expanded up to second order in ζ [22] and evaluated at the

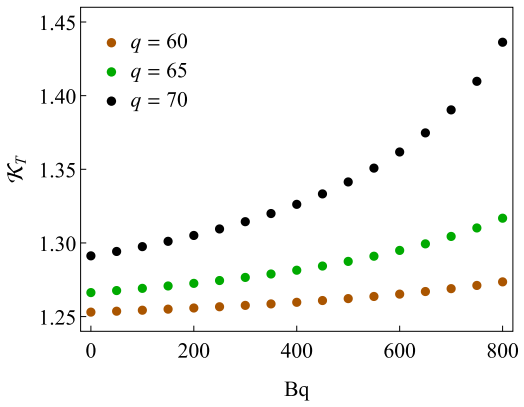

FIG. 7. Curvature of the tip of the finger indicated by small black arrows in Fig. 6, $\mathcal{K}_T$, plotted as a function of the Boussinesq number Bq. Three values of the initial aspect ratio q are considered: 60, 65, and 70, corresponding to the cases presented in Fig. 6. The curvature is evaluated at the final time $t_f = 0.56$.

angular location of the fingertip ($\theta = \theta^*$), is given by

$$\mathcal{K}_T = \left\{ \frac{1}{R} - \frac{1}{R^2}\left(\zeta + \frac{\partial^2 \zeta}{\partial \theta^2}\right) + \frac{1}{R^3}\left[\zeta^2 + \frac{1}{2}\left(\frac{\partial \zeta}{\partial \theta}\right)^2 + 2\zeta\frac{\partial^2 \zeta}{\partial \theta^2}\right]\right\}\Bigg|_{\theta=\theta^*}. \quad (18)$$

The data plotted in Fig. 7 are calculated considering the tip of the finger indicated by the black arrows in Fig. 6, located at the angle $\theta = \theta^* \approx 2\pi/5$ at the final time $t_f = 0.56$. In addition, as in Fig. 6, $q = 60$, 65, and 70. From Fig. 7, one immediately sees that, regardless of the value of q, the curvature of the fingertip increases monotonically with the Boussinesq number Bq. One can also observe that the growth of $\mathcal{K}_T$ with Bq is much more pronounced for larger values of the initial aspect ratio q. It is worth noting that we have verified that similar conclusions are reached if one evaluates the tip curvature for other inward-moving fingers of the shrinking interface. The quantitative findings extracted from Fig. 7 regarding the fingertip-sharpening behavior reinforce our previous visually based results obtained from Figs. 3, 5, and 6.

We close this section by examining yet another important morphological aspect of the lifting fingering patterns: finger competition. As commented throughout this paper, during the lifting process, the invading fingers of the outer, less viscous fluid penetrate into the inner, more viscous fluid. As time advances, the various inward-moving fingers reach different sizes and compete among themselves in their race toward the center of the cell. To investigate how finger competition events respond to interfacial rheology effects in lifting Hele-Shaw cells, we revisit Fig. 6. In Fig. 8, for each pattern shown in Figs. 6(a)–6(c) and Figs. 6(g)–6(i), we plot the radial coordinate r of each fingertip divided by the length of the largest finger $r_{\max}$ as a function of the polar coordinate θ at the final time t_f. Hence, we can compare the differences in size among the inward-moving fingers for a given pattern and contemplate how finger competition phenomena are impacted by Bq and q in a more quantitative manner than we did so far.

Figure 8 shows $r/r_{\max}$ against θ for the three values of Bq considered in Fig. 6 and two values of the initial aspect ratio: $q = 60$ in Fig. 8(a) and $q = 70$ in Fig. 8(b). In this way, Fig. 8(a) gives information about the final time interfaces in Figs. 6(a)–6(c), while Fig. 8(b) provides similar information about the corresponding last time interfaces in Figs. 6(g)–6(i). Going through Fig. 8(a), we can see that, for the smaller q, the curves for different values of Bq are quite similar and almost overlap, indicating that finger competition is not very affected by interfacial rheology effects for this lower value of q. However, when the initial aspect ratio is increased to $q = 70$ [Fig. 8(b)], so are the effects of Bq, in such a way that the relative sizes of the fingers vary more strongly as the Boussinesq number is enlarged. The curve for Bq = 0 oscillates less than the one for Bq = 500, while the curve for Bq = 800 oscillates the most. Notice that stronger oscillations in the data means more intense finger competition. Moreover, note that, even when there is no interfacial rheology, a higher q results in more finger length variability (i.e., more finger

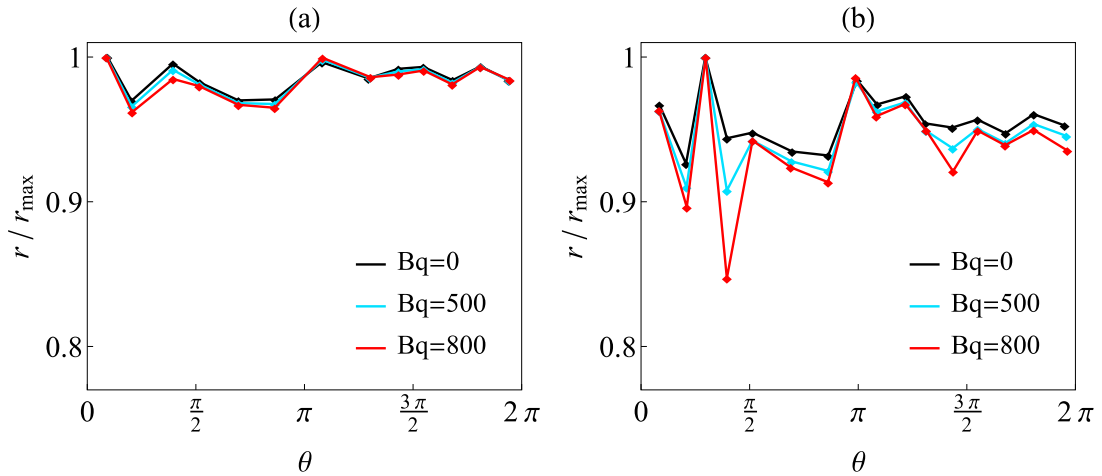

FIG. 8. Rescaled radial coordinate $r/r_{\max}$ of the fingertips for inward-moving fingers as a function of the polar angle θ, for some of the patterns illustrated in Fig. 6. Here, data are presented for (a) $q = 60$ [related to the patterns shown in Figs. 6(a)–6(c)], and (b) $q = 70$ [connected to the fingering structures displayed in Figs. 6(g)–6(i)].

competition). On the basis of such findings, we conclude that finger competition events are favored for larger values of both Bq and q.

IV. CONCLUSIONS

In this paper, we applied a perturbative second-order mode-coupling scheme to study the influence of interfacial rheology effects on the development of viscous fingering patterns in lifting Hele-Shaw cell flows. We focused on analyzing how the stability and morphology of the fingered patterns respond to different values of the Boussinesq number Bq and the initial aspect ratio q. This was done at the linear and early nonlinear regimes of the interface dynamics. Our linear results indicated an enhanced destabilization of the structured fluid-fluid interface when surface rheological effects are more intense. This is in contrast to the findings of linear stability analyses previously performed for injection-driven and centrifugally induced Hele-Shaw flows [24,28], in which interfacial rheology acts to stabilize the fluid-fluid boundary.

At the onset of nonlinearities, our second-order results have shown that interfacial rheology leads to significantly more perturbed and developed interfaces. Thus, nonlinear effects tend to enhance the destabilization behavior detected at the purely linear regime. Most importantly, our mode-coupling theory gives access to intrinsically nonlinear aspects about the morphology of the rising patterns. We have found that increasingly larger interfacial rheology effects (higher Bq) result in the formation of narrower fingered structures having sharp tip fingers. Additionally, we have detected a greater finger length variability as Bq is augmented, indicating that finger competition events are favored due to the action of surface rheological effects. Moreover, we have verified that higher values of the initial aspect ratio q (i.e., larger confinement) provoke interface destabilization, strengthening the destabilizing tendency already induced by surface rheological stresses. Finally, we have identified that the occurrence of interface recircularization at larger stages of the flow can be delayed for larger values of Bq.

We hope our linear and early nonlinear theoretical results encourage researchers to further analyze this problem, mainly at more advanced time stages of the pattern-forming dynamics, via fully nonlinear numerical simulations and experiments. Of course, these possible future studies could also be used to check the specific predictions we make in this paper.

ACKNOWLEDGMENTS

J.A.M. thanks Conselho Nacional de Desenvolvimento Científico e Tecnológico (CNPq) for financial support under Grant No. 305140/2019-1. Í.M.C. wishes to thank CNPq for financial support through Grant No. 140175/2022-9.

[1] L. M. C. Sagis, Dynamic properties of interfaces in soft matter: Experiments and theory, Rev. Mod. Phys. **83**, 1367 (2011).

[2] J. H. J. Thijssen and J. Vermant, Interfacial rheology of model particles at liquid interfaces and its relation to (bicontinuous) Pickering emulsions, J. Phys.: Condens. Matter **30**, 023002 (2018).

[3] U. T. Gonzenbach, A. R. Studart, E. Tervoort, and L. J. Gauckler, Ultrastable particle-stabilized foams, Angew. Chem. Int. Ed. **45**, 3526 (2006).

[4] J. Forth, P. Y. Kim, G. Xie, X. Liu, B. A. Helms, and T. P. Russell, Building reconfigurable devices using complex liquid-fluid interfaces, Adv. Mater. **31**, 1806370 (2019).

[5] G. G. Fuller and J. Vermant, Complex fluid-fluid interfaces: Rheology and structure, Annu. Rev. Chem. Biomol. Eng. **3**, 519 (2012).

[6] L. M. C. Sagis and E. Scholten, Complex interfaces in food: Structure and mechanical properties, Trends in Food Science and Technology **37**, 59 (2014).

[7] B. Sauerer, S. Dhahran, M. Stukan, J. Buiting, W. Abdallah, and S. Andersen, Dynamic asphaltene-stearic acid competition at the oil-water interface, Langmuir **34**, 5558 (2018).

[8] M. Caggioni, A. V. Bayles, J. Lenis, E. M. Furst, and P. T. Spicer, Interfacial stability and shape change of anisotropic endoskeleton droplets, Soft Matter **10**, 7647 (2014).

[9] H. Manikantan and T. M. Squires, Surfactant dynamics: Hidden variables controlling fluid flows, J. Fluid Mech. **892**, P1 (2020).

[10] E. Guzmán, Current perspective on the study of liquid-fluid interfaces: From fundamentals to innovative applications, Coatings **12**, 841 (2022).

[11] D. A. Edwards, H. Brenner, and D. T. Wasan, *Interfacial Transport Processes and Rheology* (Butterworth-Heinemann, Stoneham, 1991).

[12] J. C. Slattery, L. Sagis, and E.-S. Oh, *Interfacial Transport Phenomena*, 2nd ed. (Springer, Berlin, 2007).

[13] M. S. Bhamla, C. E. Giacomin, C. Balemans, and G. G. Fuller, Influence of interfacial rheology on drainage from curved surfaces, Soft Matter **10**, 6917 (2014).

[14] G. Lin, J. M. Frostad, and G. G. Fuller, Influence of interfacial elasticity on liquid entrainment in thin foam films, Phys. Rev. Fluids **3**, 114001 (2018).

[15] A. K. Sachan, S. Q. Choi, K. H. Kim, Q. Tang, L. Hwang, K. Y. C. Lee, T. M. Squires, and J. A. Zasadzinski, Interfacial rheology of coexisting solid and fluid monolayers, Soft Matter **13**, 1481 (2017).

[16] N. Singh and V. Narsimhan, Deformation and burst of a liquid droplet with viscous surface moduli in a linear flow field, Phys. Rev. Fluids **5**, 063601 (2020).

[17] N. Singh and V. Narsimhan, Numerical investigation of the effect of surface viscosity on droplet breakup and relaxation under axisymmetric extensional flow, J. Fluid Mech. **946**, A24 (2022).

[18] P. G. Saffman and G. I. Taylor, The penetration of a fluid into a porous medium or Hele-Shaw cell containing a more viscous liquid, Proc. R. Soc. London A **245**, 312 (1958).

[19] For review papers on the Saffman-Taylor instability see, for instance, G. M. Homsy, Viscous fingering in porous media, Annu. Rev. Fluid Mech. **19**, 271 (1987); K. V. McCloud and J. V. Maher, Experimental perturbations to Saffman-Taylor flow,

Phys. Rep. **260**, 139 (1995); J. Casademunt, Viscous fingering as a paradigm of interfacial pattern formation: Recent results and new challenges, Chaos **14**, 809 (2004).
[20] L. Paterson, Radial fingering in a Hele Shaw cell, J. Fluid Mech. **113**, 513 (1981).
[21] S. S. S. Cardoso and A. W. Woods, The formation of drops through viscous instability, J. Fluid Mech. **289**, 351 (1995).
[22] J. A. Miranda and M. Widom, Radial fingering in a Hele-Shaw cell: A weakly nonlinear analysis, Physica D **120**, 315 (1998).
[23] J. Li and H. Manikantan, Influence of interfacial rheology on viscous fingering, Phys. Rev. Fluids **6**, 074001 (2021).
[24] H. Conrado, E. O. Dias, and J. A. Miranda, Impact of interfacial rheology on finger tip splitting, Phys. Rev. E **107**, 015103 (2023).
[25] J. M. Boussinesq, Existence of a surface viscosity, in the thin transition layer separating a liquid from another contiguous fluid, Ann. Chim. Phys. **29**, 349 (1913).
[26] L. E. Scriven, Dynamics of a fluid interface equation of motion for Newtonian surface fluids, Chem. Eng. Sci. **12**, 98 (1960).
[27] L. E. Scriven and C. V. Sternling, The Marangoni effects, Nature (London) **187**, 186 (1960).
[28] I. M. Coutinho, E. O. Dias, and J. A. Miranda, Effect of interfacial rheology on fingering patterns in rotating Hele-Shaw cells, Phys. Rev. E **107**, 025105 (2023).
[29] Ll. Carrillo, F. X. Magdaleno, J. Casademunt, and J. Ortín, Experiments in a rotating Hele-Shaw cell, Phys. Rev. E **54**, 6260 (1996).
[30] E. Alvarez-Lacalle, J. Ortín, and J. Casademunt, Low viscosity contrast fingering in a rotating Hele-Shaw cell, Phys. Fluids **16**, 908 (2004).
[31] R. Folch, E. Alvarez-Lacalle, J. Ortín, and J. Casademunt, Pattern formation and interface pinch-off in rotating Hele-Shaw flows: A phase-field approach, Phys. Rev. E **80**, 056305 (2009).
[32] L. C. Morrow, T. J. Moroney, and S. W. McCue, Numerical investigation of controlling interfacial instabilities in a non-standard Hele-Shaw configurations, J. Fluid Mech. **877**, 1063 (2019).
[33] M. J. Shelley, F. Tian, and K. Wlodarski, Hele-Shaw flow and pattern formation in a time-dependent gap, Nonlinearity **10**, 1471 (1997).
[34] T. Dutta, S. K. Kabiraj, S. Sinha, and S. Tarafdar, Radially interrupted viscous fingers in a lifting Hele-Shaw cell, Eur. Phys. J. B **36**, 297 (2003).
[35] S. K. Kabiraj and S. Tarafdar, Finger velocities in the lifting Hele-Shaw cell, Physica A **328**, 305 (2003).
[36] M. Ben Amar and D. Bonn, Fingering instabilities in adhesive failure, Physica D **209**, 1 (2005).
[37] A. Lindner, D. Derks, and M. J. Shelley, Stretch flow of thin layers of Newtonian liquids: Fingering patterns and lifting forces, Phys. Fluids **17**, 072107 (2005).
[38] S. Sinha, T. Dutta, and S. Tarafdar, Adhesion and fingering in the lifting Hele-Shaw cell: Role of the substrate, Eur. Phys. J. E **25**, 267 (2008).
[39] J. Nase, D. Derks, and A. Lindner, Dynamic evolution of fingering patterns in a lifted Hele-Shaw cell, Phys. Fluids **23**, 123101 (2011).
[40] Z. Zheng, H. Kim, and H. A. Stone, Controlling Viscous Fingering Using Time-Dependent Strategies, Phys. Rev. Lett. **115**, 174501 (2015).
[41] C. Vaquero-Stainer, M. Heil, A. Juel, and D. Pihler-Puzovic, Self-similar and disordered front propagation in a radial Hele-Shaw channel with time-varying cell depth, Phys. Rev. Fluids **4**, 064002 (2019).
[42] M. Zhao, Z. Niroobakhsh, J. Lowengrub, and S. Li, Nonlinear limiting dynamics of a shrinking interface in a Hele-Shaw cell, J. Fluid Mech. **910**, A41 (2021).
[43] L. C. Morrow, T. J. Moroney, M. C. Dallaston, and S. W. McCue, A review of one-phase Hele-Shaw flows and a level-set method for non-standard configurations, ANZIAM J. **63**, 269 (2021).
[44] P. H. A. Anjos, E. O. Dias, L. Dias, and J. A. Miranda, Adhesion force in fluids: Effects of fingering, wetting, and viscous normal stresses, Phys. Rev. E **91**, 013003 (2015).
[45] H. K. Moffatt, H. Guest, and H. E. Huppert, Spreading or contraction of viscous drops between plates: Single, multiple or annular drops, J. Fluid Mech. **925**, A26 (2021).
[46] T. U. Islam and P. S. Gandhi, Viscous fingering in multiport Hele-Shaw cell for controlled shaping of fluids, Sci. Rep. **7**, 16602 (2017).
[47] S. D. Kanhurkar, V. Patankar, T. U. Islam, P. S. Gandhi, and A. Bhattacharya, Stability of viscous fingering in lifted Hele-Shaw cells with a hole, Phys. Rev. Fluids **4**, 094003 (2019).
[48] E. Alvarez-Lacalle, E. Pauné, J. Casademunt, and J. Ortín, Systematic weakly nonlinear analysis of radial viscous fingering, Phys. Rev. E **68**, 026308 (2003).
[49] E. Alvarez-Lacalle, J. Casademunt, and J. Ortín, Systematic weakly nonlinear analysis of interfacial instabilities in Hele-Shaw flows, Phys. Rev. E **64**, 016302 (2001).
[50] J. A. Miranda and E. Alvarez-Lacalle, Viscosity contrast effects on fingering formation in rotating Hele-Shaw flows, Phys. Rev. E **72**, 026306 (2005).
[51] C.-Y. Chen, C.-H. Chen, and J. A. Miranda, Numerical study of pattern formation in miscible rotating Hele-Shaw flows, Phys. Rev. E **73**, 046306 (2006).
[52] C.-Y. Chen, Y.-S. Huang, and J. A. Miranda, Diffuse-interface approach to rotating Hele-Shaw flows, Phys. Rev. E **84**, 046302 (2011).
[53] P. H. A. Anjos and S. Li, Weakly nonlinear analysis of the Saffman-Taylor problem in a radially spreading fluid annulus, Phys. Rev. Fluids **5**, 054002 (2020).
[54] M. Zhao, P. H. A. Anjos, J. Lowengrub, and S. Li, Pattern formation of the three-layer Saffman-Taylor problem in a radial Hele-Shaw cell, Phys. Rev. Fluids **5**, 124005 (2020).
[55] R. M. Oliveira and J. A. Miranda, Fully nonlinear simulations of ferrofluid patterns in a radial magnetic field, Phys. Rev. Fluids **5**, 124003 (2020).
[56] Z. Yu and I. C. Christov, Tuning a magnetic field to generate spinning ferrofluid droplets with controllable speed via nonlinear periodic interfacial waves, Phys. Rev. E **103**, 013103 (2021).
[57] R. M. Oliveira, I. M. Coutinho, P. H. A. Anjos, and J. A. Miranda, Shape instabilities in confined ferrofluids under crossed magnetic fields, Phys. Rev. E **104**, 065113 (2021).
[58] J. A. Miranda and R. M. Oliveira, Time-dependent gap Hele-Shaw cell with a ferrofluid: Evidence for an interfacial singularity inhibition by a magnetic field, Phys. Rev. E **69**, 066312 (2004).
[59] H. Kim, T. Funada, D. D. Joseph, and G. M. Homsy, Viscous potential flow analysis of radial fingering in a Hele-Shaw cell, Phys. Fluids **21**, 074106 (2009).

[60] I. M. Coutinho, F. M. Rocha, and J. A. Miranda, Viscous normal stresses and fingertip tripling in radial Hele-Shaw flows, Phys. Rev. E **104**, 045106 (2021).

[61] T. Verwijlen, P. Moldenaers, H. A. Stone, and J. Vermant, Study of the flow field in the magnetic rod interfacial stress rheometer, Langmuir **27**, 9345 (2011).

[62] Z. A. Zell, A. Nowbahar, V. Mansard, L. G. Leal, S. S. Deshmukh, J. M. Mecca, C. J. Tucker, and T. M. Squires, Surface shear inviscidity of soluble surfactants, Proc. Natl. Acad. Sci. USA **111**, 3677 (2014).

[63] N. Jaensson and J. Vermant, Tensiometry and rheology of complex interfaces, Curr. Opin. Colloid Interface Sci. **37**, 136 (2018).

[64] A. P. Kotula and S. L. Anna, Insoluble layer deposition and dilatational rheology at a microscale spherical cap interface, Soft Matter **12**, 7038 (2016).

[65] D. Georgieva, V. Schmitt, F. Leal-Calderon, and D. Langevin, On the possible role of surface elasticity in emulsion stability, Langmuir **25**, 5565 (2009).

[66] T. J. Stoodt and J. C. Slattery, Effect of the interfacial viscosities upon displacement, AIChE J. **30**, 564 (1984).

[67] D. M. A. Buzza, C.-Y. D. Lu, and M. E. Cates, Linear shear rheology of incompressible foams, J. Phys. II France **5**, 37 (1995).

[68] M. J. P. Gingras and Z. Rácz, Noise and the linear stability analysis of viscous fingering, Phys. Rev. A **40**, 5960 (1989).